Luminescence Properties of Samarium-Doped Hydroxyapatite Nanoparticles and Cytotoxicity Assessment on SH-SY5Y Neuroblastoma Cells

Stephanie Enríquez, Sarah Briceño,* Lenin Ramirez-Cando, Alexis Debut, Luis J. Borrero-González, and Gema González*

Cite This: ACS Omega 2024, 9, 49857−49866

Read Online

ACCESS | Metrics & More | Article Recommendations

ABSTRACT: Samarium-doped nanohydroxyapatite is a biomaterial with nerve regeneration activity and bioimaging. In this work, Sm/HAp; $(Ca_{10-x}Sm_x(PO_4)_6(OH)_2)$ $(0 \leq x \leq 1)$ was synthesized using the hydrothermal method and thermally treated from 200 to 800 °C. The samples were characterized by transmission electron microscopy, energy-dispersive X-ray spectroscopy, Fourier transform infrared spectroscopy, X-ray diffraction, Raman spectroscopy, and luminescence spectroscopy. The results confirmed the successful integration of Sm^{3+} ions into the hydroxyapatite. Our findings revealed the influence of the Sm^{3+} content and thermal treatment on the emission properties, obtaining a maximum emission at Sm = 0.05 thermally treated at 800 °C. The SH-SY5Y neuroblastoma cell viability study revealed a Sm^{3+} concentration-and particle size-dependent response. This research emphasizes the optical and cell viability of Sm/HAp in SH-SY5Y neuroblastoma cells, making them suitable for further research as agents that activate regenerative processes in cells and neurons.
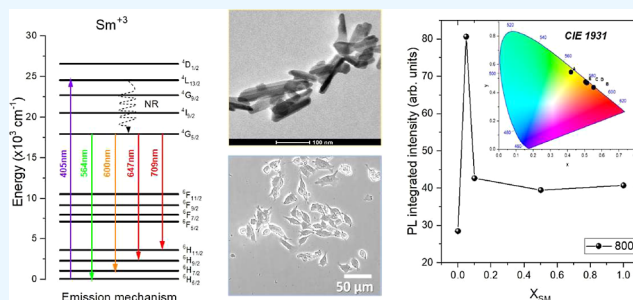
INTRODUCTION

Hydroxyapatite (HAp) is a commonly used biomaterial in biomedical applications and is the main constituent of bone tissue.[1,2] This inorganic compound exhibits an affinity for substitutions, which enhances its unique properties. By replacing Ca^{2+} ions with lanthanides, the material gains improved optical,[3] antimicrobial, and biological characteristics.[4] In particular, samarium (Sm^{3+}) possesses a strong affinity for bone minerals, making it suitable for bioimaging and drug-delivery systems, rendering samarium-doped hydroxyapatite (Sm/HAp) a focal point in numerous research studies.

Biocompatibility studies using Sm/HAp nanoparticles in HeLa cell lines revealed efficient cellular uptake and reduced toxicity at lower Sm^{3+} doping concentrations. The combination of enhanced luminescence and favorable biocompatibility positions Sm/HAp as a promising in vitro imaging agent.[5] Sm/HAp has been extensively investigated as a potential coating for implants, primarily due to its antimicrobial properties. Implant failure often results from bacterial adhesion and biofilm formation, leading to infections. Turculet et al., Iconaru et al., and Ciobanu et al. successfully developed antifungal Sm/HAp films to study the proliferation of *Candida albicans* ATCC 10231 fungal strain. In particular, higher concentrations of Sm^{3+} exhibited greater antifungal activity.[6−8]

The effect of lanthanide ions on nerve regeneration remains a matter of dispute. Moreover, lanthanide ions have long and photostable emissions and could be used in bioimaging in real-time.[9] Samarium-doped hydroxyapatite has been effectively tested in various cell lines, including HGF-1 gingival fibroblasts,[10] hFOB 1.19 osteoblasts,[3] and HeLa cervical cancer-derived cells.[11] The neurodegenerative activity of HAp has been studied in vivo and in vitro, confirming a strong regenerative property.[12−14] SH-SY5Y: The Human Neuroblastoma Cell Line is commonly used as a model for neurodegenerative disorders. In addition, the SH-SY5Y cell line has been widely used in experimental neurological studies, including the analysis of neuronal differentiation, metabolism, and function related to neurodegenerative processes, neurotoxicity, and neuroprotection.[15] In this work, samarium-doped hydroxyapatite (x_{Sm} = 0.05, 0.1, 0.5, 1.0), thermally treated from 200 to 800 °C have been used to evaluate emission

properties and cell viability in SH-SY5Y neuroblastoma cells. Our findings showed that the emission properties were influenced by the Sm^{3+} content and the thermal treatment. We found that the maximum emission occurred when the Sm^{3+} content was 0.05 and thermally treated at 800 °C. Furthermore, the cell viability study on SH-SY5Y neuroblastoma cells indicated that the response was dependent on both the Sm^{3+} content [3+] and the particle size.

MATERIALS AND METHODS

Chemicals. The precursors for synthesizing the samarium-doped hydroxyapatite nanoparticles were supplied by Sigma-Aldrich (St. Louis, Missouri, United States). These include calcium chloride ($CaCl_2$, ACS reagent, ≥99%), diammonium hydrogen phosphate [$(NH_4)_2HPO_4$, reagent grade, ≥98%], and ammonium hydroxide [$(NH_4)OH$]. Furthermore, Sm^{3+} ions for doping come from samarium(III) nitrate hexahydrate [$Sm(NO_3)_3\cdot6H_2O$] with a purity of 99.9% trace metals basis.

Essential components for cell culture and maintenance were supplied by Gibco, a division of Thermo Fisher Scientific (Waltham, Massachusetts, United States). These included Dulbecco's modified Eagle's medium (DMEM), fetal bovine serum (FBS), penicillin–streptomycin antibiotic, phosphate buffered saline solution (PBS), and 0.25% trypsin–EDTA. Gibco also supplied the 0.4% trypan blue solution for the Trypan Blue technique.

Synthesis of Samarium-Doped Hydroxyapatite Nanoparticles. Samarium-doped hydroxyapatite nanoparticles [$Ca_{10-x}Sm_x(PO_4)_6(OH)_2$, x_{Sm} = (0.05, 0.10, 0.50, 1.00)] were synthesized by the hydrothermal method with (Ca + Sm)/P fixed to 1.67. For the synthesis, $(NH_4)_2HPO_4$ was dissolved in 25 mL of distilled water. A 25 mL of $CaCl_2$ and $Sm(NO_3)_3\cdot6H_2O$ solution was added dropwise from a buret to the $(NH_4)_2HPO_4$ solution in constant agitation at room temperature. After that, 5 mL of $(NH_4)OH$ was added to the resulting solution to increase the pH from 5 to 10. Then, it was mounted on a reactor and placed on the stove at 125 °C for 24 h. The sample was washed with distilled water until the pH dropped to 7. Then, it was dried on the stove at 60 °C for 48 h. Finally, the sample was calcined at 200, 400, 600, and 800 °C. The concentrations and masses of the compounds are described in Table 1.

Table 1. Concentration and Masses of the Compounds Following the Fixed (Ca + Sm)/P = 1.67

cCa^{2+} (mmol)	cSm^{3+} (mmol)	$c(PO_4)^{3-}$ (mmol)	mCa^{2+} (g)	mSm^{3+} (g)	$m(PO_4)^{3-}$ (g)
10.00	0.00	5.98	1.1098	0.0000	0.7898
9.95	0.05	5.98	1.1042	0.0222	0.7898
9.90	0.10	5.98	1.0987	0.0444	0.7898
9.50	0.50	5.98	1.0543	0.2222	0.7898
9.00	1.00	5.98	0.9988	0.4445	0.7898

Characterization. The vibrational bands within the structure of samarium-doped hydroxyapatite were studied using Fourier transform infrared (FTIR) spectroscopy using a Cary 630 FTIR spectrometer with Diamond ATR accessory (Agilent Technologies, Inc.). The Raman spectra were obtained using a LabRAM HR Evolution Confocal Raman Microscope (HORIBA). Raman spectra were obtained with acquisition times of 5 s, and the samples were excited by using a 633 nm He–Ne laser. The crystalline structure of the Sm/

HAp powders was identified by X-ray diffraction (XRD) using a MiniFlex benchtop X-ray diffractometer (Rigaku Corporation), with monochromatic $CuK\alpha$ radiation (λ = 1.5418 Å). Transmission electron micrographs were obtained at 120 kV by using an FEI-Tecnai G20 Spirit microscope with an Eagle 4k HR camera. A multifunctional optical system was used to measure the photoluminescence (PL) spectra. The PL spectra were collected in the visible region using a diode laser with a wavelength of 405 nm as the excitation source. The emission signals were dispersed by a monochromator (140 mm Czerny-Turner, MicroHR, Horiba) and detected with a dual Si/InGaAs solid-state detector [DSS-SIGA(2.2)020A, Horiba]. Signal digitization was performed using a data acquisition system (SpectrAcq3, Horiba) controlled by SynerJY software (Horiba).

Cytotoxicity Studies. Cytotoxic effects were evaluated using Trypan Blue Dye Exclusion and MTT assays. Human neuroblastoma cells (SH-SY5Y) were cultured in DMEM medium complemented with 10% FBS and 1% penicillin–streptomycin in a CO_2 incubator at 37 °C with 5% CO_2. Cell growth was monitored by using a Motic AE31E inverted microscope (Motic China Group Co., Hong Kong, China). After 48 h of incubation, cells were treated with a 10 mg/L dilution of Sm/HAp sample powders mixed with a 0.9% sterile sodium chloride saline solution (LIFE, Quito, Ecuador). Cells treated with HAp and untreated cells were used as controls.

The Trypan Blue test assesses cell viability on the basis of the ability of live cells to exclude the dye. In contrast, dead cells take up the dye because of the compromised membrane integrity. In this study, cells were cultured at a concentration of 5000 cells per well in a 48-well plate, with each well containing 400 μL of culture medium. After a 48 h incubation, 10 μL of treatments and 40 μL of DMSO were added. The test was carried out 24 h after treatment by adding 100 μL of a 0.4% trypan blue solution to each well, followed by a 10 min incubation at room temperature. After that, the well contents were discarded and the cells were observed and counted using an inverted microscope.

Data Analysis. Data were presented as the mean value ±standard deviation (SD). Statistical analysis involved conducting one-way analysis of variance (ANOVA) followed by Dunnett's posthoc test, with a significance level of p < 0.05. All statistical analyses were performed using the R software.

RESULTS AND DISCUSSION

Structural Characterization. *Transmission Electron Microscopy.* Transmission electron micrographs of the samples Sm/HAp (x_{Sm} = 0, 0.05 and 0.5) uncalcined and thermally treated at 800 °C are presented in Figure 1. In this figure, the hydroxyapatite nanoparticles have a rod shape with an average length of 100 nm and a width of 30 nm. The average width of the Sm/HAp samples decreases from 30 to 15 nm when the samarium content increases at room temperature due to inhibition of hydroxyapatite crystallization with Sm^{3+} doping.[16,17] After the thermal treatment of the samples at 800 °C, it is observed that the average particle size increases from 30 nm width to 100 nm due to the diffusion process at 800 °C to form larger particles[18] and the morphology changes from rods to spherical particles with smoother edges.

XRD. In Figure 2a, the XRD pattern of Sm/HAp samples calcined at 200 °C is presented. All diffraction peaks correspond to the hexagonal phase of pure hydroxyapatite with $P6_3/m$ spatial symmetry, as well as the main characteristic
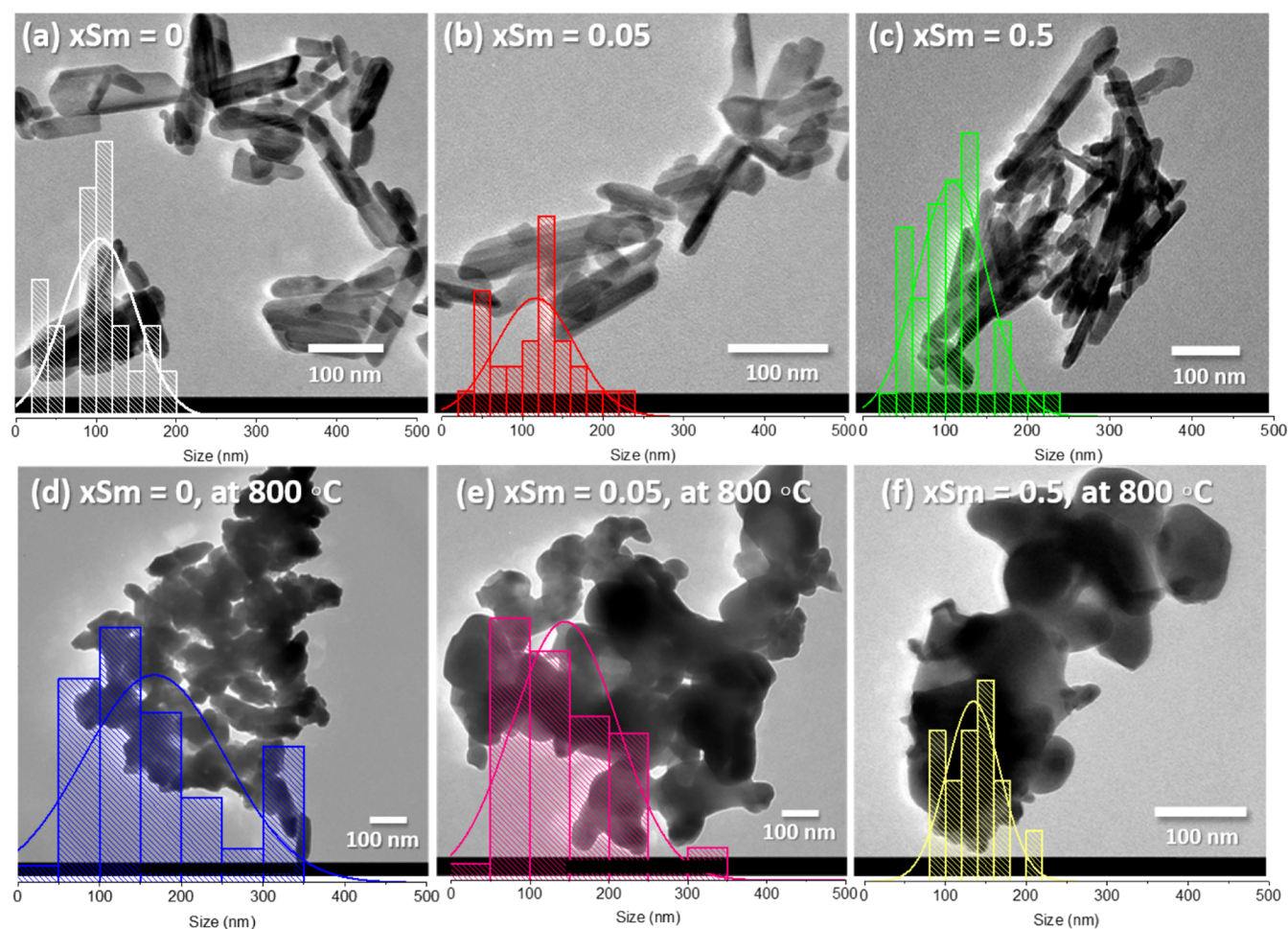
Figure 1. Transmission electron micrographs and histograms of (a) $x_{Sm} = 0$, (b) $x_{Sm} = 0.05$, (c) $x_{Sm} = 0.5$, and samples thermally treated at 800 °C for (d) $x_{Sm} = 0$, (e) $x_{Sm} = 0.05$, and (f) $x_{Sm} = 0.5$.

peaks occurring at the diffraction angles of 25.8, 31.7, 32.8, 34.1, 39.7, 46.7, 49.4, and 53.1°.[19] These angles align with the crystal planes (002), (211), (300), (202), (130), (222), (213), and (004) from the standard pattern (COD Card: 00−900−2214). Furthermore, the diffraction data show distinct and well-defined peaks for samples with up to $x_{Sm} = 0.5$, and no additional peaks suggestive of secondary phases or impurities were detected.[11,19] These results demonstrate that the substitution of Sm^{3+} ions for Ca^{2+} ions occurred successfully without altering the crystal structure of hydroxyapatite.[3,11] However, at higher Sm^{3+} concentrations, additional peaks and changes in the peak intensity suggest a distorted network.

In addition, upon substituting Sm^{3+} for Ca^{2+} ions, the diffraction peaks exhibit an apparent shift toward larger angles, accompanied by peak broadening. This shift is attributed to the introduction of smaller Sm^{3+} ions ($r_{ion} = 1.079$) compared to Ca^{2+} ions ($r_{ion} = 1.260$), resulting in a contraction of the crystal spacing. Smaller ions typically lead to closer atomic packing, causing decreases in interatomic distances and alterations in the angles between crystal planes. This decrease in the interatomic distance is reflected in the XRD pattern as a shift toward larger 2θ angles, which agrees with Bragg's law. Consequently, the broadening of the peaks observed with increased Sm^{3+} concentration can be attributed to a reduction in particle size.[3] A progressive decrease in the intensity of the diffraction peaks is also observed with an increase in the Sm^{3+}

concentration as a result of disorder within the crystal lattice and a nonuniform distribution of Sm^{3+} ions, potentially as a result of partial occupancy, resulting in weaker diffraction peaks.

Consistent behavior is observed for the samples thermally treated from 200 to 600 °C. However, at 800 °C, additional peaks emerge in all samarium concentrations, indicating a phase transformation. These diffraction peaks align well with trigonal tricalcium phosphate (TCP) using hexagonal axes with a $R3c$/H symmetry group, as per ICDD no. 00−151−7238. XRD peaks of TCP are identified at 27.7, 29.5, 30.9, 34.2, and 52.8°, corresponding to the (1010), (300), (0210), (220), and (2020) lattice planes, respectively. Notably, a partial phase change to β-TCP occurs for pure HAp and every samarium content. The increase in the Sm^{3+} content improves both the appearance and intensity of the TCP diffraction peaks, with the exception of $x_{Sm} = 0.05$, which exhibits a high degree of phase transformation. Phase transformations of calcium phosphates with temperature have been well studied, and the formation of the whitlockite phase $Ca_3(PO_4)_2$, β-TCP has been reported at temperatures above 750 °C[20,21] [7−14]. The mechanism of phase transformation of Hap to TCP at high temperatures involves the formation of oxyhydroapatite and oxyapatite with a gradual release of OH^- ions above 700 °C.[22]

FTIR Spectroscopy. Figure 3a presents the FTIR spectra of Sm/HAp at varying samarium concentrations under 200 °C

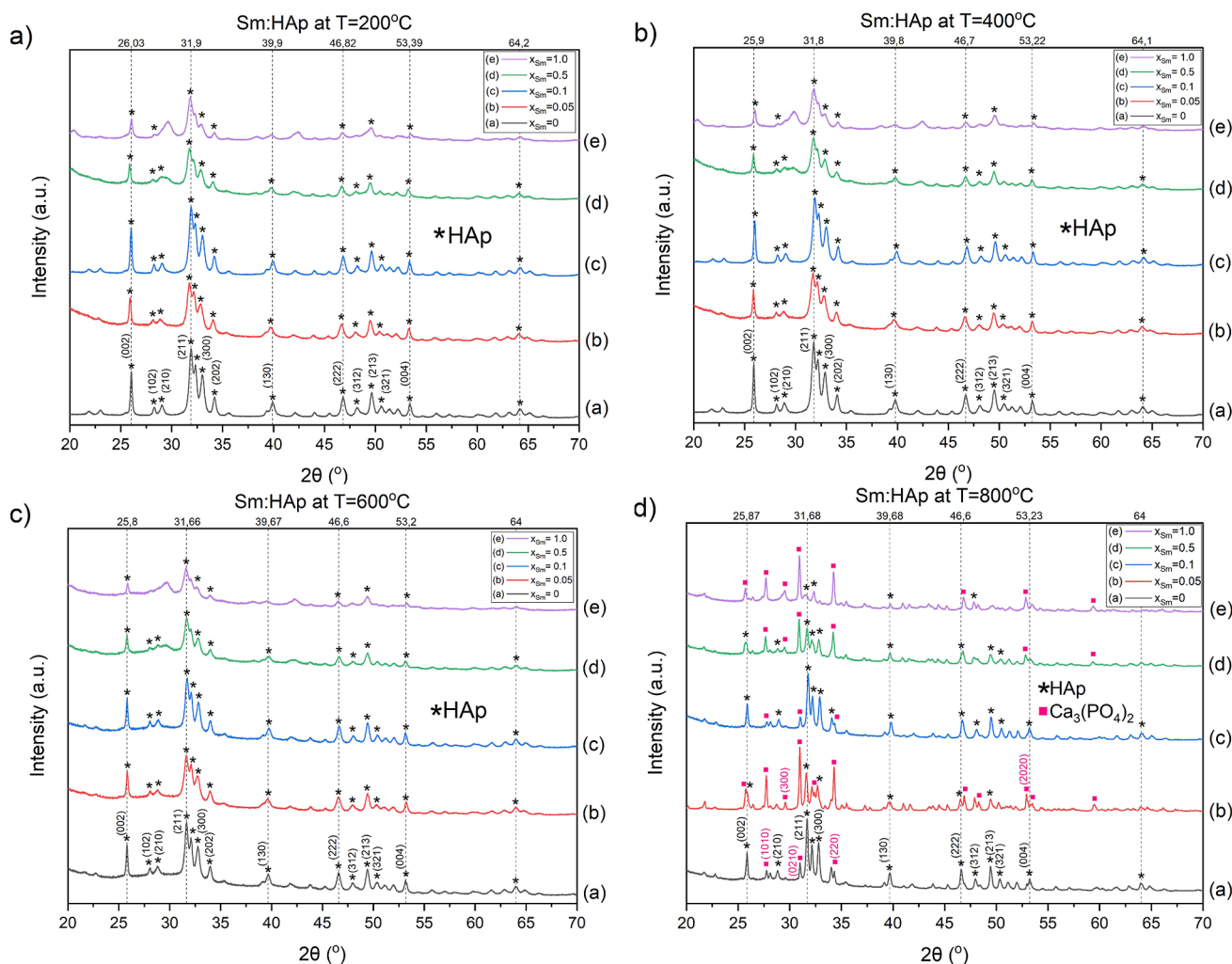**Figure 2.** XRD pattern of Sm/HAp at different samarium concentrations (x_{Sm} = 0, 0.05, 0.1, 0.5, and 1.0) for different calcination temperatures: (a) 200 °C, (b) 400 °C, (c) 600 °C, and (d) 800 °C.

calcination. As reported in the literature, the bands centered around 630 and 3570 cm^{-1} correspond to the vibrational (ν_L) and stretching (ν_s) vibrational modes of hydroxyl, respectively.[23] The presence of these bands suggests a well-crystallized structure.[10,11] The vibrations associated with the phosphate group are the peaks at approximately 1020 and 1088 cm^{-1} attributed to the triply degenerated asymmetric stretching vibration (ν_3) of the P−O bond; the shoulder at 961 cm^{-1} assigned to the nondegenerated symmetric stretching vibration (ν_1) of the P−O bond; the peaks at 560 and 600 cm^{-1} designated to the triply degenerated bending mode (ν_4) of the O−P−O bond; and a weak peak at ~473 cm^{-1} ascribed to the double degenerated bending mode (ν_2).[24] The vibrational peak at 1626 cm^{-1} corresponds to the H−O−H bending mode of water, as well as the region between 3000 and 3600 cm^{-1},[10,11,23] observed at x_{Sm} = 1.0. At this concentration, a small band at 1425 cm^{-1} emerges, indicating a C−O vibration (ν_3), characteristic of the carbonate group $(CO_3)^{2-}$. Bands specific to the hydrogen phosphate group $(HPO_4)^{2-}$ are found at around 870 cm^{-1}.[24] An additional peak for $(HPO_4)^{2-}$ is identified at ~533 cm^{-1} for x_{Sm} = 1.0.[23]

As observed, the regions corresponding to the bands at 1088, 960, 872, 630, and 475 cm^{-1} exhibit a decreasing contribution when the concentration of samarium is increased in the samples. When x_{Sm} = 1.0, these bands are almost absent.

The disappearance and shifts of these peaks may be attributed to the introduction of Sm^{3+} ions. The increasing concentration of samarium induces structural changes in HAp, affecting the local environment within the crystal lattice and the vibrational properties of specific regions. Similar behavior is evident in Sm/HAp samples calcined at 400, 600, and 800 °C, as illustrated in Figure 3b−d. However, the $\nu_3(CO_3)^{2-}$ band at 1425 cm^{-1} disappears from 400 °C onward, and the O−H water band at 1626 cm^{-1} vanishes at 600 °C. This phenomenon may be attributed to a gradual decomposition or release of entrapped species during the heating process. At 800 °C, the $(HPO_4)^{2-}$ peaks disappear completely. In addition, changes in the peak shapes corresponding to the phosphate group are observed in these samples. They resemble the peak shape of β-tricalcium phosphate (β-TCP, β-$Ca_3(PO_4)_2$),[25] suggesting a partial phase change occurring at 800 °C for x_{Sm} = 0.05, 0.5, 1.0.

Raman Spectroscopy. Figure 4a illustrates the Raman spectra of Sm/HAp samples thermally treated at 200 °C, with the corresponding experimental band positions and assignments. The most prominent band, observed at 962 cm^{-1}, is attributed to the ν_1 symmetric stretching vibrational mode of the P−O bond in $(PO_4)^{3-}$. Nearby, peaks at 1047 and 1077 cm^{-1} correspond to the ν_3 asymmetric stretching mode of the P−O bond. At lower wavenumbers, the 430−452 cm^{-1} range
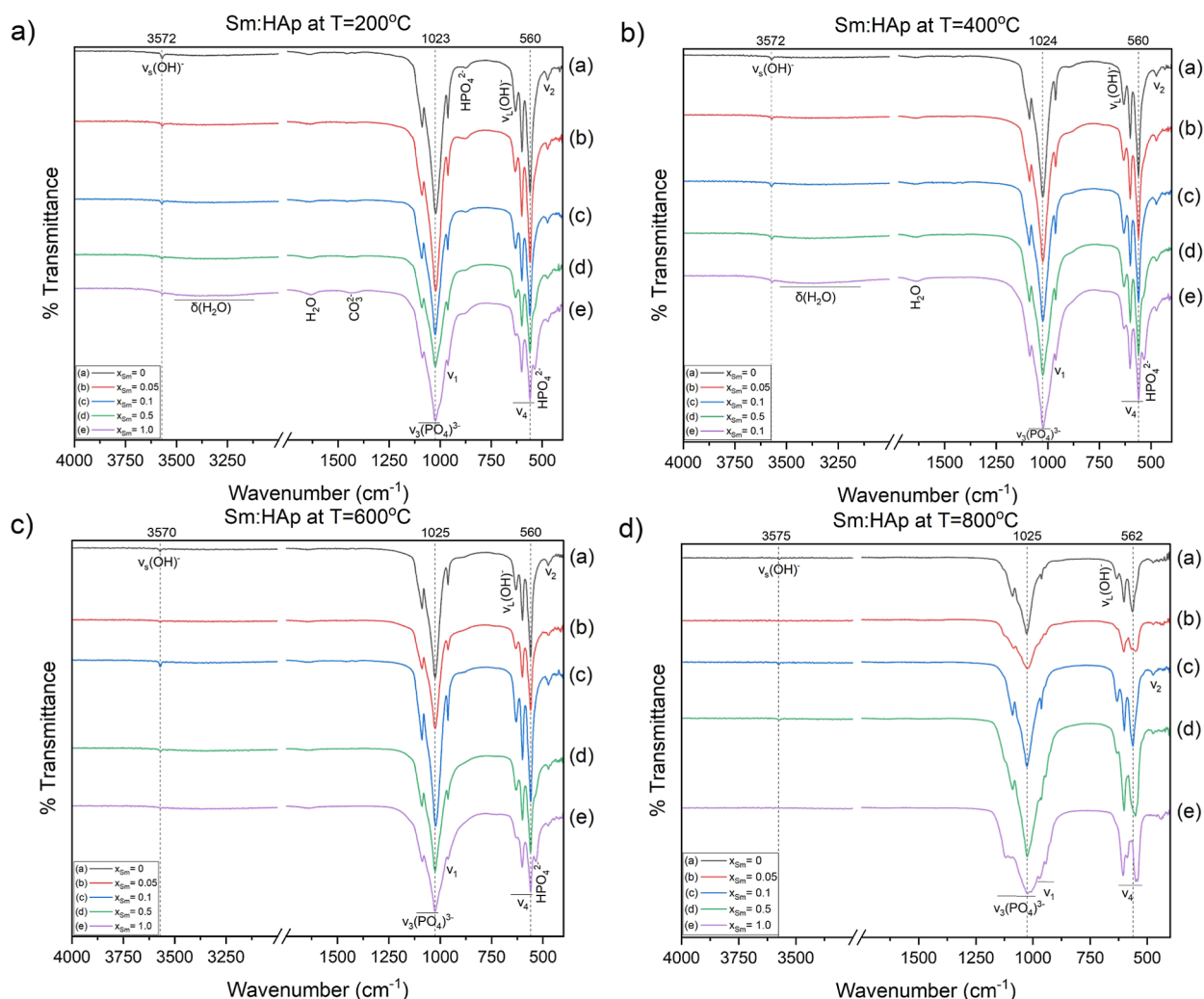
Figure 3. FTIR spectra of Sm/HAp at different Sm^{3+} concentrations (x_{Sm} = 0, 0.05, 0.1, 0.5, and 1.0) for different calcination temperatures: (a) 200 °C, (b) 400 °C, (c) 600 °C, and (d) 800 °C.

and the 592−607 cm^{-1} range are associated with the bending vibrations ν_2 and ν_4 of O−P−O, respectively.[26−28] The literature reports that ν_1 peaks in the 962−964 cm^{-1} range indicates a highly crystalline HAp.[29]

Similar results are observed on samples calcined at 400, 600, and 800 °C, as depicted in Figure 4b−d. Nonetheless, at certain dopant concentrations and calcination temperatures, specific bands at 430, 590, and 1048 cm^{-1} corresponding to ν_2, ν_4, and ν_3, respectively, disappear. The absence of these bands may be associated with a decrease in crystallinity, alterations in crystal size, or changes in the local environment, as was observed with XRD for high samarium concentrations. At 800 °C, the peak shapes in the ν_1 region change due to the presence of an additional peak at 971 cm^{-1} with high intensity in samples with x_{Sm} = 0.05 and 0.1. According to the literature, a vibrational mode at ∼969 cm^{-1}, accompanied by a wide band at 940−950 cm^{-1}, corresponds to the β-TCP spectrum,[30] suggesting a partial conversion of HAp to β-TCP consistent with the XRD results.

Photoluminescence Spectroscopy. The luminescence properties of the Sm^{3+}/HAp samples were analyzed by using PL spectroscopy. Figure 5a shows the PL spectra in the visible region for Sm^{3+}/HAp nanoparticles thermally treated at 200 °C under 405 nm excitation. As observed, undoped

hydroxyapatite exhibits a low signal in this region. On the other hand, samarium-doped nanoparticles display an emission spectrum with bands centered at 564, 600, 647, and 709 nm. These bands are assigned to the well-known electronic transitions within the Sm^{3+} ion: $^4G_{5/2} \rightarrow {}^6H_{J/2}$ (J = 5, 7, 9, and 11)[19,31,32] and illustrated in the energy level diagram of Sm^{3+} ion in Figure 6a. Sm^{3+} reaches its strongest relative PL intensity at 600 nm in the visible region, producing an orange-light emission. Similar results are reported in the literature for Sm^{3+}-doped HAp.[19] The Sm^{3+} emission mechanism is explained as follows: upon laser excitation at 405 nm, the incident photon promotes electron transition from the $^6H_{5/2}$ ground state level to the $^4L_{13/12}$ higher energy level, after that a nonradiative relaxation process from the $^4L_{13/2}$ level to the $^4G_{5/2}$ level occurs. Afterward, there are radiative transitions from the $^4G_{5/2}$ level to the $^6H_{J/2}$ (J = 5, 7, 9, 11) levels.

Among the various Sm^{3+} concentrations, x_{Sm} = 0.05 has the highest emission intensity due to the presence of TCP phase observed at this composition from 200 to 800 °C by XRD. Additionally, Sm^{3+} ions replaced Ca^+ ions within the hydroxyapatite structure with the formation of vacancies to compensate for charge balance and maintain electrical neutrality, producing emission enhancement. As the concentration of Sm^{3+} increases, a decrease in luminescence is
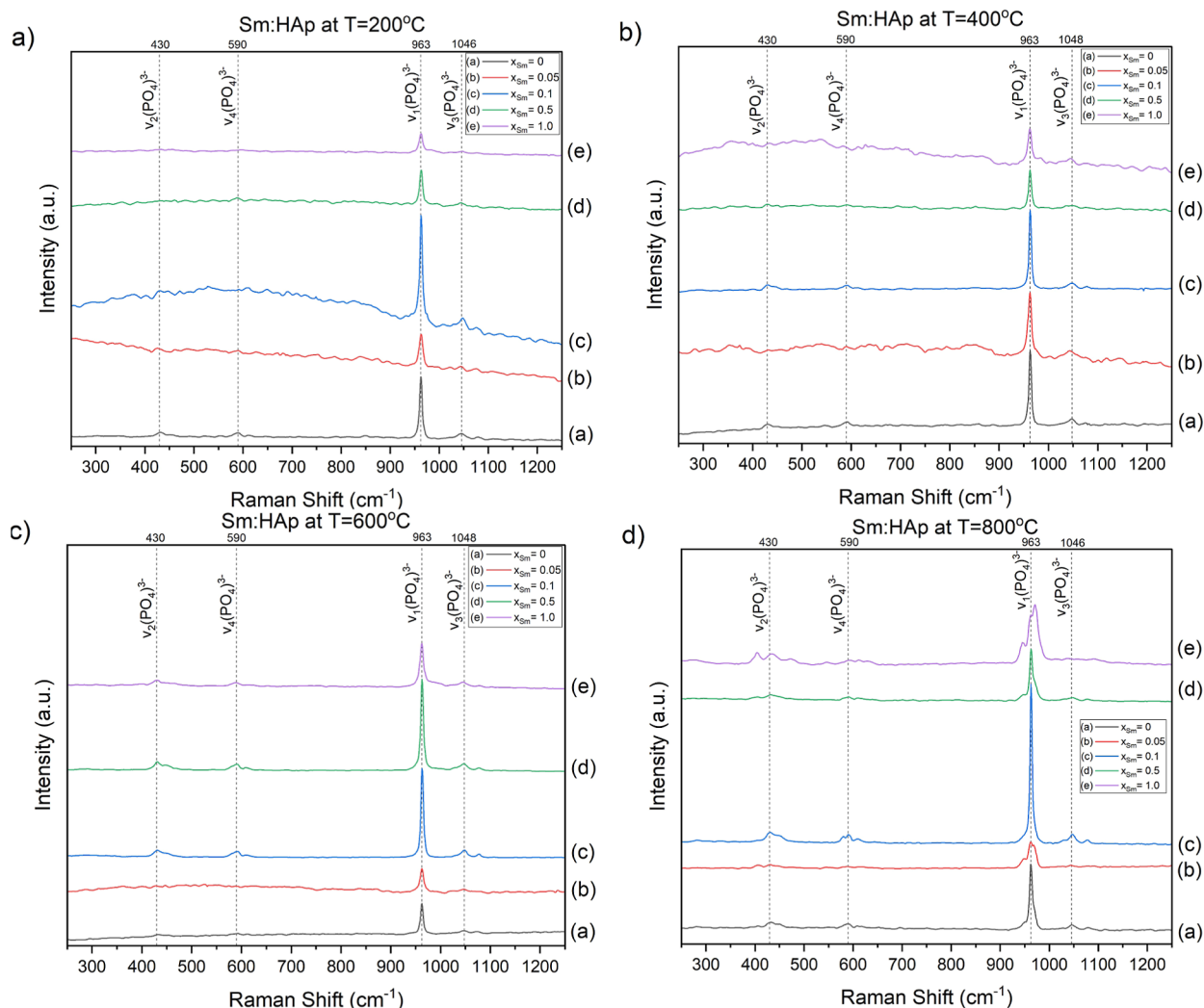
Figure 4. Raman spectra of Sm/HAp at different Sm^{3+} concentrations (x_{Sm} = 0, 0.05, 0.1, 0.5, and 1.0) for different calcination temperatures: (a) 200 °C, (b) 400 °C, (c) 600 °C, and (d) 800 °C.

observed due to the concentration quenching effects. This Sm^{3+} concentration quenching is reported in, for example, Sm^{3+}-doped HAp,[19,31] Sm^{3+}-doped yttrium aluminum borate phosphors,[33] and Sm^{3+}-doped tellurite-germanate glasses.[34]

As illustrated in Figure 5b−d, consistent trends are observed across the Sm/HAp nanoparticles thermally treated from 200 to 800 °C. Minimal variability in emission intensity is evident across different dopant concentrations for all temperatures. However, a pronounced increase in PL intensity occurs for the thermally treated samples at 800 °C. FTIR and XRD analyses indicate a phase transformation to -TCP at this temperature. Such phase transformations are typically related to structural and electronic alterations, along with changes in defect concentration and enhanced emission intensity.[17]

In order to search for the color perception of Sm/HAp samples, the Commission International de I'Eclairage (CIE) 1931 chromaticity coordinates (X, Y) have been determined using the PL spectra.[35] The CIE chromatic color coordinates are essential parameters to measure the quality of the luminescent color. The values of CIE color coordinates of the thermally treated samples at 800 °C excited under 405 nm were calculated and are illustrated in the inset of Figure 6b. For x_{Sm} = 0 (X: 0.421, Y: 0.546)—label A, x_{Sm} = 0.05 (X: 0.552, Y: 0.438)—label B, x_{Sm} = 0.1 (X: 0.510, Y: 0.472)—label C, x_{Sm} =

0.5 (X: 0.513, Y: 0.470)—label D, and x_{Sm} = 1.0 (X: 0.504, Y: 0.477)—label E. These results indicate a color change from green-yellow (for the undoped sample) to an orange color (for the doped samples). Sample x_{Sm} = 0.05 is the one that emits more orange color. Also, the integrated intensities were calculated with the PL spectra for the samples thermally treated at 800 °C and were plotted as a function of the Sm^{3+} concentration. The results are shown in Figure 6b, evidencing the existence of Sm^{3+} concentration quenching for concentrations greater than 0.05. These mechanisms that quench the Sm^{3+} emission with concentration are illustrated in Figure 6a, specifically the following transitions: $^4G_{5/2} \rightarrow {}^6F_{11/2}$, $^6H_{5/2} \rightarrow {}^6F_{5/2}$ (CR1), $^4G_{5/2} \rightarrow {}^6F_{9/2}$, $^6H_{5/2} \rightarrow {}^6F_{7/2}$ (CR2), $^4G_{5/2} \rightarrow {}^6F_{7/2}$, $^6H_{5/2} \rightarrow {}^6F_{9/2}$ (CR3), $^4G_{5/2} \rightarrow {}^6F_{5/2}$, $^6H_{5/2} \rightarrow {}^6F_{11/2}$ (CR4), known as cross-relaxation (CR) mechanisms between neighbor Sm^{3+} ions.[33,34] At x_{Sm} = 0.05, the energy-transfer processes in the samarium-doped hydroxyapatite structure are optimized because of the formation of vacancies to compensate for the charge balance.

Cytotoxicity Studies. *Trypan Blue Dye Exclusion.* The Trypan Blue Dye Exclusion test was used for a quantitative assessment of membrane integrity after 24 h exposure. As shown in Figure 7, the viability of cells exposed to both undoped and doped samples exhibited dose−response changes
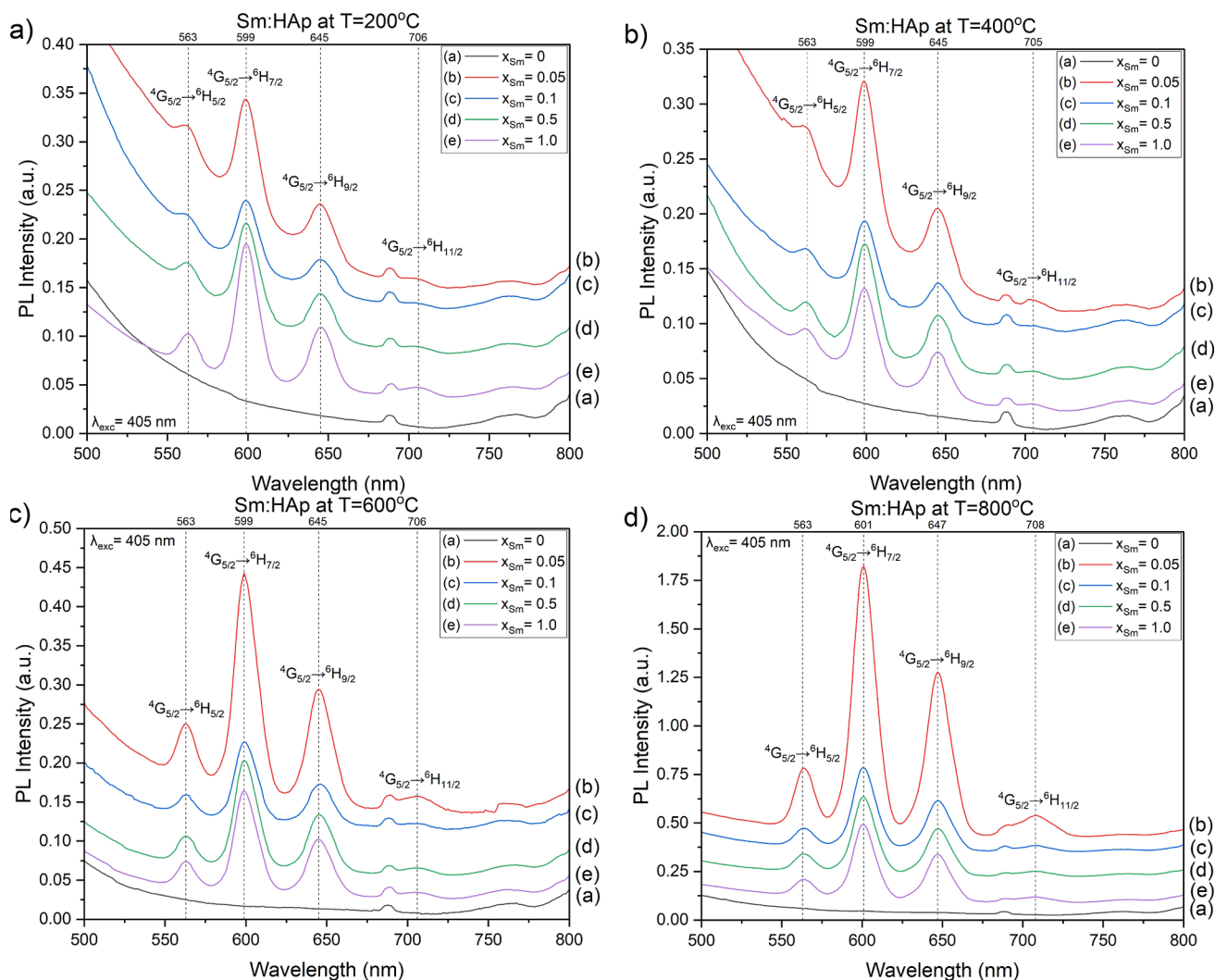
Figure 5. PL spectra of Sm/HAp at different samarium concentrations (x_{Sm} = 0, 0.05, 0.1, 0.5, and 1.0) for different calcination temperatures: (a) 200 °C, (b) 400 °C, (c) 600 °C, and (d) 800 °C.

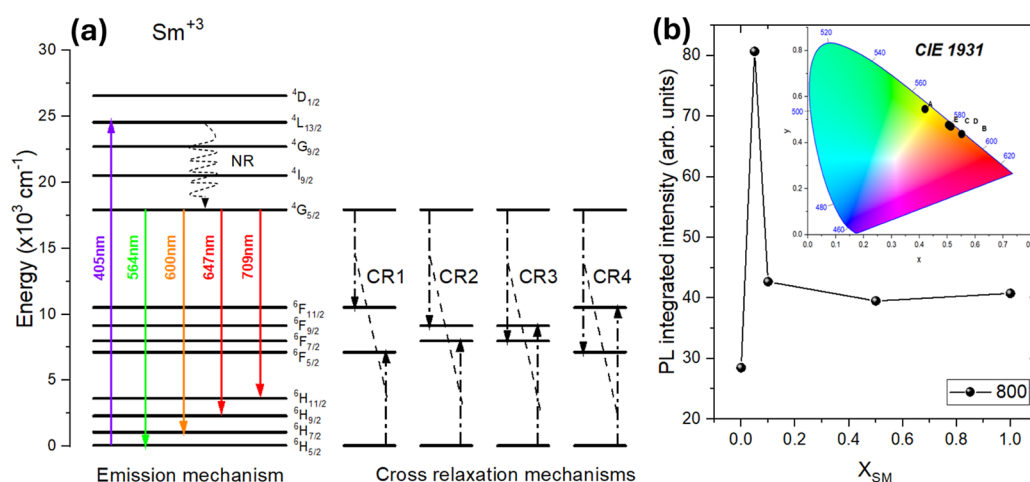**Figure 6.** . (a) Energy level diagram of Sm3+, (b) PL integrated intensity of the thermally treated samples at 800 ∘C upon excitation at 405 nm. The inset presents the CIE color coordinates.

(F = 20.18 on 21 and 88 DF, p-value = < 2.2×10^{-16}). Hydroxyapatite, compared to the control with 93.26% cell viability, showed a slight decrease at 92.63%; this difference is not significant with Dunnett's test p-value = 0.85. For x_{Sm} =

0.05, 0.1, 0.5, and 1.0 at room temperature, the geometric average viabilities were 88.78%, 84.55%, 84.99%, and 83.98%, respectively, indicating a concentration-dependent reduction in cell viability for Sm/HAp samples. The same trend is observed
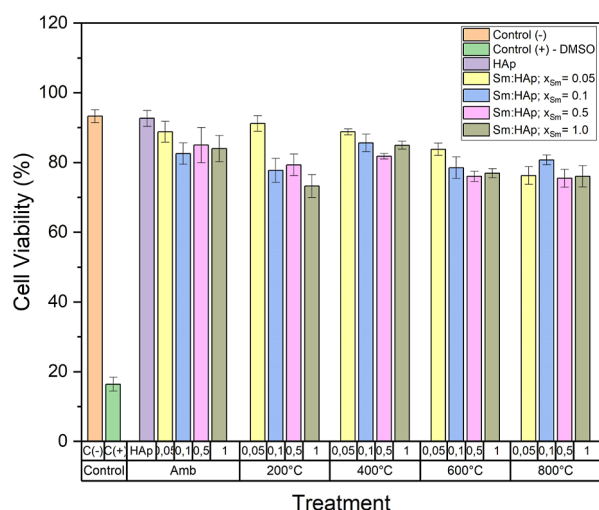
Figure 7. Cell viability assessment using Trypan Blue Dye Exclusion test: percentage of viable SH-SY5Y cells after a 24 h incubation with Sm/HAp nanoparticles (x_{Sm} = 0, 0.05, 0.1, 0.5, and 1.0) calcined at different temperatures. Results are expressed as the mean ± SD.

for different temperatures. Although a slight decrease is evident for the samples thermally treated, further analysis is needed to determine a definitive pattern. Complementary, the variance analysis further indicates that concentration, temperature and their interaction have a significant effect on the results with F-values of 3.55, 13.76 and 6.42, respectively, and corresponding p-values of 0.05, 3.4 × 10^5, and 4.58 × 10^{-8} approximately. These findings suggest that both the concentration of Sm/HAp and the calcination temperature significantly influence cell viability in a crescent dose−response manner (Figures 7 and 8). However, further studies are needed to confirm these observations.

Balas et al.[36] reported that HAp and SmHAp nanoparticles showed biocompatibility at concentrations below 25 and 50 μg/mL, respectively, for exposure periods up to 72 h. Additionally, these authors found that cell membrane integrity remained intact following treatment with concentrations as high as 100 μg/mL for HAp and 400 μg/mL for SmHAp, underscoring the role of Sm^{3+} ions in enhancing HAp's cytocompatibility. This is in good agreement with our results indicating that SmHAp nanoparticles provide a modest but beneficial influence on cell viability for all the concentrations studied (0.05 to 1 atom %) and for all the particle sizes (L = 84

to 182 nm) from rodlike to spherical morphologies, obtained at the different temperatures treatments (25 to 800 °C). The higher temperature particles with spherical morphology and larger particle size presented a slightly lower viability compared to HAp nanoparticles but still around 80% and cell migration. Notably, the effect of Sm^{3+} concentration on hydroxyapatite did not show any adverse impact on viability for any particle size. These findings suggest that Sm^{3+} ions in HAp highlight the potential role of Sm^{3+} ions as a significant contribution to biomedical applications focused on bone regeneration and bioimaging applications.

On the other hand, at high temperatures, partial or total transformation (800 °C) of Hap to TCP was observed in XRD. Several authors have investigated the effect of TCP on cytotoxicity, and they found no observable cytotoxicity for these materials, similar to hydroxyapatite.[37] Additionally, it has been reported in invitro and in vivo studies that composites HAp/TCP stimulate bone formation greater than that of pure Hap. This is attributed to the rapid resorption of β-TCP, which enhances vascularization and promotes increased bone formation.[38] The better biosorption of β-tricalcium phosphate β-Ca$_3$(PO$_4$)$_2$, β-TCP due to its greater solubility than HAp in physiological environments has been reported.[39]

Microscopic observations of SH-SY5Y cells in Figure 8 show the morphological differences between the (+) control (Figure 8a) and (−) control-DMSO in Figure 8. The morphology of SH-SY5Y cells in the (+) control exhibits a neurite outgrowth and takes on a neuron-like appearance. Meanwhile, the cells in control (−) maintain their standard morphology, representing small, round, and undifferentiated cells when in their proliferative state. In Figure 8c,e, cells in the presence of 5 μL of HAp and Sm/HAp x_{Sm} = 0.05 are observed to show the cell's morphology to proliferate in agreement with the (+) control. The samples in Figure 7d, Sm/HAp x_{Sm} = 0.5 at 600 °C, and Figure 8f Sm/HAp x_{Sm} = 0.5 present some round cells representing a decrease in cell viability due to the samarium content and thermal treatment.

Our results revealed that the particle size and chemical composition of samarium-doped hydroxyapatite influence cell viability. Primarily, trypan blue is used to assess the viability by measuring the permeability of the dye on deceased cells, indicating damaged cell membranes. There have been reported that Ln^{3+} ions perforate the cell membrane even at low concentrations. Higher doses of Ln^{3+} ions activate apoptosis genes or cause DNA cleavage, resulting in observable cytotoxic effects at both cellular and animal in vivo levels. At lower
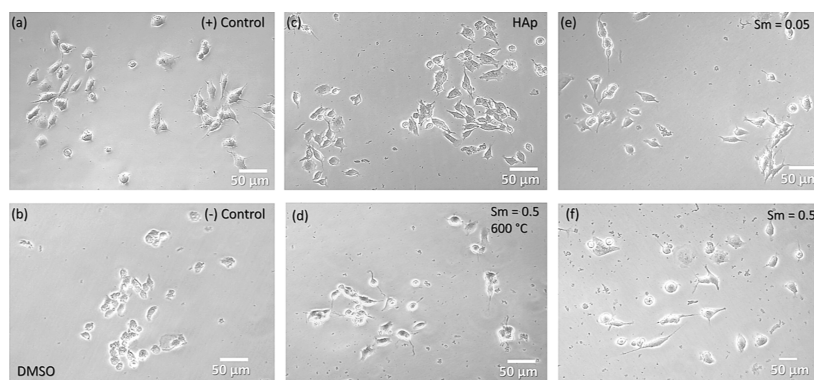

Figure 8. Microscopic observations of SH-SY5Y cells (a) (+) control, (b) (−) control-DMSO, (c) HAp, (d), HApx_{Sm} = 0.5 at 600 °C, (e) HApx_{Sm} = 0.05, and (f) HApx_{Sm} = 0.5.

concentrations, lanthanides exhibit positive effects such as scavenging reactive oxygen species, providing cell protection, stabilizing the cytoskeleton, and improving immunological responses.[40] In this context, the dye exclusion test indicated a reduction in the percentages of viable cells in cultures exposed to Sm/HAp compared with those exposed to pure HAp.

Several physical properties, including size, morphology, aggregation state, and surface texture, also influence biological effects. When particle size is considered, the interaction between particles and the plasma membrane is crucial. Smaller particles exhibit efficient interfacial interaction with the cell membrane, leading to enhanced particle intake compared with that of larger particles. Consequently, smaller particles generally show lower toxicity, while larger particles tend to reduce cell viability.[41] The latter is consistent with our observations, where smaller particles were obtained at room temperature and the average particle size increased with the thermal treatment. In the viability study, there is a trend to increase the cytotoxicity with increasing samarium concentration and temperature. However, at 800 °C, this observation raises the possibility that the particle size may be more important than the Sm^{3+} content, as observed in Figure 7. Therefore, our results reveal that in the case of neurotoxicity in SH-SY5Y cells, the Sm/HAp samples exhibit elevated cell viability and minimal neurotoxicity in terms of membrane integrity for all Sm^{3+} concentrations and calcination temperatures.

CONCLUSIONS

The formation of Sm/HAp with different Sm^{3+} contents showed an increase in particle size with the calcination temperature. The optimal Sm^{3+} content was 0.05 at 800 °C, with an increase in the intensity of the PL emission. Cell viability in SH-SY5Y neuroblastoma cells is affected by the particle size and the formation of TCP-HAp. Preliminary biological studies reveal that Sm-HAp exhibits elevated cell viability and minimal neurotoxicity for all Sm^{3+} concentrations studied and calcination temperatures. Therefore, these materials could be attractive for neuroregeneration with real-time bioimaging.

AUTHOR INFORMATION

Corresponding Authors

Sarah Briceño − *School of Physical Sciences and Nanotechnology, Yachay Tech University, Urcuquí 100119, Ecuador;* orcid.org/0000-0002-4004-4951; Email: sarahbriara@gmail.com

Gema González − *School of Physical Sciences and Nanotechnology, Yachay Tech University, Urcuquí 100119, Ecuador;* orcid.org/0000-0003-4526-2429; Email: gemagonz@yachaytech.edu.ec

Authors

Stephanie Enríquez − *School of Physical Sciences and Nanotechnology, Yachay Tech University, Urcuquí 100119, Ecuador;* orcid.org/0009-0000-7836-067X

Lenin Ramirez-Cando − *School of Biological Sciences and Engineering, Yachay Tech University, Urcuquí 100119, Ecuador*

Alexis Debut − *Centro de Nanociencia y Nanotecnología, Universidad de las Fuerzas Armadas ESPE, Sangolquí 171103, Ecuador;* orcid.org/0000-0002-8269-7619

Luis J. Borrero-González − *Facultad de Ciencias Exactas y Naturales, Escuela de Ciencias Físicas y Matemática, Laboratorio de Optica Aplicada, Pontificia Universidad Católica del Ecuador, Quito 170525, Ecuador;* orcid.org/0000-0003-3853-5433

Complete contact information is available at:
https://pubs.acs.org/10.1021/acsomega.4c08654

Notes

The authors declare no competing financial interest.

REFERENCES

(1) Murugan, N.; Sundaramurthy, A.; Chen, S.-M.; Sundramoorthy, A. K. Graphene oxide/oxidized carbon nanofiber/mineralized hydroxyapatite based hybrid composite for biomedical applications. *Mater. Res. Express* **2017**, *4*, 124005.

(2) Murugan, N.; Murugan, C.; Sundramoorthy, A. K. In vitro and in vivo characterization of mineralized hydroxyapatite/polycaprolactone-graphene oxide based bioactive multifunctional coating on Ti alloy for bone implant applications. *Arabian J. Chem.* **2018**, *11*, 959−969.

(3) Ciobanu, C.; Iconaru, S.; Popa, C.; Motelica-Heino, M.; Predoi, D. Evaluation of samarium doped hydroxyapatite, ceramics for medical application: Antimicrobial activity. *J. Nanomater.* **2015**, *2015*, 14.

(4) Iconaru, S. L.; Groza, A.; Gaiaschi, S.; Rokosz, K.; Raaen, S.; Ciobanu, S. C.; Chapon, P.; Predoi, D. Antimicrobial properties of samarium doped hydroxyapatite suspensions and coatings. *Coatings* **2020**, *10*, 1124.

(5) Zantye, P.; Fernandes, F.; Ramanan, S. R.; Kowshik, M. Rare earth doped hydroxyapatite nanoparticles for in vitro bioimaging applications. *Curr. Phys. Chem.* **2019**, *9*, 94−109.

(6) Turculet, C. S.; Prodan, A. M.; Negoi, I.; Teleanu, G.; Popa, M.; Andronescu, E.; Beuran, M.; Stanciu, G. A.; Hristu, R.; Badea, M. L. Preliminary evaluation of the antifungal activity of samarium doped hydroxyapatite thin films. *Rom. Biotechnol. Lett.* **2018**, *23*, 13928−13932.

(7) Iconaru, S.; Stanciu, G.; Hristu, R.; Ghita, R. Properties of samarium doped hydroxyapatite thin films deposited by evaporation. *Rom. Rep. Phys.* **2017**, *69*, 508.

(8) Ciobanu, C. S.; Predoi, D.; Chapon, P.; Predoi, M. V.; Iconaru, S. L. Fabrication and Physico-Chemical Properties of Antifungal Samarium Doped Hydroxyapatite Thin Films. *Coatings* **2021**, *11*, 1466.

(9) Doat, A.; Pellé, F.; Gardant, N.; Lebugle, A. Synthesis of luminescent bioapatite nanoparticles for utilization as a biological probe. *J. Solid State Chem.* **2004**, *177*, 1179−1187.

(10) Nica, I. C.; Popa, M.; Marutescu, L.; Dinischiotu, A.; Iconaru, S. L.; Ciobanu, S. C.; Predoi, D. Biocompatibility and antibiofilm properties of samarium doped hydroxyapatite coatings: An in vitro study. *Coatings* **2021**, *11*, 1185.

(11) Ciobanu, S. C.; Iconaru, S. L.; Predoi, D.; Prodan, A. M.; Predoi, M. V. Physico-chemical properties and in vitro antifungal evaluation of samarium doped hydroxyapatite coatings. *Coatings* **2020**, *10*, 827.

(12) Wiatrak, B.; Sobierajska, P.; Szandruk-Bender, M.; Jawien, P.; Janeczek, M.; Dobrzynski, M.; Pistor, P.; Szelag, A.; Wiglusz, R. J. Nanohydroxyapatite as a Biomaterial for Peripheral Nerve Regeneration after Mechanical Damage—In Vitro Study. *Int. J. Mol. Sci.* **2021**, *22*, 4454.

(13) Liu, M.; Zhou, G.; Song, W.; Li, P.; Liu, H.; Niu, X.; Fan, Y. Effect of nano-hydroxyapatite on the axonal guidance growth of rat cortical neurons. *Nanoscale* **2012**, *4*, 3201−3207.

(14) Nawrotek, K.; Makiewicz, M.; Zawadzki, D. Fabrication and Characterization of Polycaprolactone/Chitosan—Hydroxyapatite Hybrid Implants for Peripheral Nerve Regeneration. *Polymers* **2021**, *13*, 775.

(15) Xicoy, H.; Wieringa, B.; Martens, G. J. The SH-SY5Y cell line in Parkinson's disease research: a systematic review. *Mol. Neurodegener.* **2017**, *12*, 10−11.

(16) Ciobanu, C. S.; Iconaru, S. L.; Massuyeau, F.; Constantin, L. V.; Costescu, A.; Predoi, D. Synthesis, structure, and luminescent properties of europium-doped hydroxyapatite nanocrystalline powders. *J. Nanomater.* **2012**, *2012*, 61.

(17) Vega-Zerpa, M. F.; Briceño, S.; Bahamonde-Duarte, J.; Vizuete, K.; Debut, A.; Uribe, R.; Borrero-González, L. J.; González, G. Optical and structural properties of Europium-doped hydroxyapatite. *Ceram. Int.* **2024**.

(18) Garcia Dominguez, G.; Hernández, A. G.; Montes, G. C.; Ramírez, A. M.; Torre, S. D. D. L. Structural and Luminescent Properties of Europium-Doped and Undoped Hydroxyapatite Powders Sintered by Spark Plasma. *Ceram.-Silik.* **2019**, *63*, 100−109.

(19) Chen, P.; Wang, F.; Qiao, Y.; Zhang, Z. Luminescence of samarium doped hydroxyapatite containing strontium: Effects of doping concentration. *J. Rare Earths* **2022**, *40*, 398−405.

(20) Böhme, N.; Hauke, K.; Dohrn, M.; Neuroth, M.; Geisler, T. High-temperature phase transformations of hydroxylapatite and the formation of silicocarnotite in the hydroxylapatite−quartz−lime system studied in situ and in operando by Raman spectroscopy. *J. Mater. Sci.* **2022**, *57*, 15239−15266.

(21) Lebugle, A.; Zahidi, E.; Bonel, G. Effect of structure and composition on the thermal decomposition of calcium phosphates (Ca/P= 1.33). *React. Solids* **1986**, *2*, 151−161.

(22) Coelho, J. M.; Moreira, J. A.; Almeida, A.; Monteiro, F. J. Synthesis and characterization of HAp nanorods from a cationic surfactant template method. *J. Mater. Sci.: Mater. Med.* **2010**, *21*, 2543−2549.

(23) Ciobanu, C. S.; Popa, C. L.; Predoi, D. Sm/HAp Nanopowders Present Antibacterial Activity against *Enterococcus faecalis*. *J. Nanomater.* **2014**, *2014*, 6.

(24) Frumosu, F.; Iconaru, S.; Predoi, D. Europium concentration effect of europium doped hydroxyapatite on proliferation of osteoblast cells. *Dig. J. Nanomater. Biostruct* **2011**, *6*, 1859−1865.

(25) Afriani, F.; Dahlan, K.; Nikmatin, S.; Zuas, O. Alginate affecting the characteristics of porous beta-TCP/alginate composite scaffolds. *J. Optoelectron. Adv. Mater.* **2015**, *7*, 67−76.

(26) Garskaite, E.; Gross, K.-A.; Yang, S.-W.; Yang, T. C.-K.; Yang, J.-C.; Kareiva, A. Effect of processing conditions on the crystallinity and structure of carbonated calcium hydroxyapatite (CHAp). *CrystEngComm* **2014**, *16*, 3950−3959.

(27) Ciobanu, C. S.; Iconaru, S. L.; Le Coustumer, P.; Constantin, L. V.; Predoi, D. Antibacterial activity of silver-doped hydroxyapatite nanoparticles against gram-positive and gram-negative bacteria. *Nanoscale Res. Lett.* **2012**, *7*, 324−329.

(28) Cancelliere, R.; Rea, G.; Micheli, L.; Mantegazza, P.; Bauer, E. M.; El Khouri, A.; Tempesta, E.; Altomare, A.; Capelli, D.; Capitelli, F. Electrochemical and Structural Characterization of Lanthanum-Doped Hydroxyapatite: A Promising Material for Sensing Applications. *Materials* **2023**, *16*, 4522.

(29) Timchenko, P.; Timchenko, E.; Pisareva, E.; Vlasov, M. Y.; Volova, L.; Frolov, O.; Kalimullina, A. Experimental studies of hydroxyapatite by Raman spectroscopy. *J. Opt. Technol.* **2018**, *85*, 130−135.

(30) Başak, T.; Hasan, T.; Feray, B.; Enes, A. M.; Abdulgani, T.; Ivana, C.; Ahmet, H.; Kenan, C.; Di, S. A.; Adil, M. Synthesis and in vitro toxicity assessment of different nano-calcium phosphate nanoparticles. *Braz. Arch. Biol. Technol.* **2022**, *65*..

(31) Lv, Y.; Shi, Q.; Jin, Y.; Ren, H.; Qin, Y.; Wang, B.; Song, S. Preparation and Luminescent Properties of the antibacterial materials of the La^{3+} Doped Sm^{3+}-Hydroxyapatite. *J. Phys.:Conf. Ser.* **2018**, *986*, 012010.

(32) Carnall, W.; Fields, P.; Rajnak, K. Electronic energy levels in the trivalent lanthanide aquo ions. I. Pr^{3+}, Nd^{3+}, Pm^{3+}, Sm^{3+}, Dy^{3+}, Ho^{3+}, Er^{3+}, and Tm^{3+}. *J. Chem. Phys.* **1968**, *49*, 4424−4442.

(33) Jamalaiah, B. C.; Rasool, S. N. Fluorescence properties of Sm3+ ions in yttrium aluminum borate phosphors for optical applications. *J. Mol. Struct.* **2015**, *1097*, 161−165.

(34) Alvarez-Ramos, M. Luminescence and study of channels for cross-relaxation dependent on the concentration of Sm^{3+} under simultaneous UV-IR excitation in tellurite-germanate glasses. *J. Alloys Compd.* **2021**, *854*, 157076.

(35) Godlewski, M.; Skrobot, M.; Guziewicz, E.; Phillips, M. Color tuning of white light emission from thin films of ZnSe. *J. Lumin.* **2007**, *125*, 85−91.

(36) Balas, M.; Badea, M. A.; Ciobanu, S. C.; Piciu, F.; Iconaru, S. L.; Dinischiotu, A.; Predoi, D. Biocompatibility and Osteogenic Activity of Samarium-Doped Hydroxyapatite—Biomimetic Nanoceramics for Bone Regeneration Applications. *Biomimetics* **2024**, *9*, 309.

(37) da Silva Brum, I.; de Carvalho, J. J.; da Silva Pires, J. L.; de Carvalho, M. A. A.; dos Santos, L. B. F.; Elias, C. N. Nanosized hydroxyapatite and β-tricalcium phosphate composite: Physicochemical, cytotoxicity, morphological properties and in vivo trial. *Sci. Rep.* **2019**, *9*, 19602.

(38) Kojima, S.; Nakamura, H.; Lee, S.; Nagata, F.; Kato, K. Hydroxyapatite Formation on Self-Assembling Peptides with Differing Secondary Structures and Their Selective Adsorption for Proteins. *Int. J. Mol. Sci.* **2019**, *20*, 4650.

(39) Xie, Y.; Chopin, D.; Morin, C.; Hardouin, P.; Zhu, Z.; Tang, J.; Lu, J. Evaluation of the osteogenesis and biodegradation of porous biphasic ceramic in the human spine. *Biomaterials* **2006**, *27*, 2761−2767.

(40) Wang, K.; Li, R.; Cheng, Y.; Zhu, B. Lanthanides—the future drugs? *Coord. Chem. Rev.* **1999**, *190*, 297−308.

(41) Shi, Z.; Huang, X.; Cai, Y.; Tang, R.; Yang, D. Size effect of hydroxyapatite nanoparticles on proliferation and apoptosis of osteoblast-like cells. *Acta Biomater.* **2009**, *5*, 338−345.